Highly ordered Pd, Fe, and Co clusters on alumina on $Ni_3Al(111)$

Andreas Buchsbaum,[1] Maurizio De Santis,[2] Helio C. N. Tolentino,[2] Michael Schmid,[1] and Peter Varga[1]
[1]*Institut für Angewandte Physik, Technische Universität Wien, A-1040 Wien, Austria*
[2]*Institut Neel, CNRS and UJF, BP 166, 38042 Grenoble Cedex 9, France*
(Received 12 November 2009; revised manuscript received 3 February 2010; published 11 March 2010)

Template-mediated growth of metals has attracted much interest due to the remarkable magnetic and catalytic properties of clusters in the nanometer range and provides the opportunity to grow clusters with narrow size distributions. We have grown well-ordered Fe and Co clusters on the ultrathin aluminum oxide on $Ni_3Al(111)$, a template with a 4.1 nm lattice. The structure of the ≈0.5-nm-thick oxide film exhibits holes reaching down to the metal substrate at the corners of the $(\sqrt{67}\times\sqrt{67})R12.2°$ unit cell. Pd atoms trapped in these corner holes create metallic nucleation sites where Fe as well as Co clusters can nucleate and form a well-ordered hexagonal arrangement on the oxide nanomesh. We have studied these Fe and Co clusters and applied different methods such as scanning tunneling microscopy and surface x-ray diffraction to determine the morphology and crystallography of the clusters. For Fe, we found cluster growth in either bcc[110] or bcc[100] direction, depending on the deposition temperature and for Co we found close-packed planes on top of the clusters and random stacking of close-packed planes. Pd clusters grow with fcc(111) orientation.

DOI: 10.1103/PhysRevB.81.115420 PACS number(s): 68.47.Jn, 61.46.Df, 68.47.Gh, 81.16.Dn

I. INTRODUCTION

Template-mediated growth of metals has attracted much interest not only due to the remarkable magnetic properties[1–18] but also due to catalytic properties[19–28] of clusters in the nanometer range. Intrinsic properties of bulk materials change as soon as surface and interface effects start to play a role.[1,3,4,7,10,11] Templates are not only a means to grow regularly arranged clusters but also provide the opportunity to grow clusters with a narrow size distribution by simple evaporation, taking advantage of the fact that the capture zones of equidistant clusters have equal area. Other techniques such as colloidal chemistry, soft landing from the gas phase, or deposition of clusters from the liquid phase give less control over either the arrangement or the size distribution of the clusters. Thus, self-assembly on template surfaces is a perfect way of growing well-defined arrays of nanoclusters.[3,14,15,17,29–34]

Nanoparticles (e.g., colloidal Co nanoparticles[35,36]) used in catalysis offer not only the advantage of a large surface area available for the catalytic reaction but also the presence of catalytically active sites on different facets and on the edges of the nanoparticle.[27,28] Recent studies of oxide-supported metal nanoparticles show an enhanced catalytic activity of nanoparticles in the presence of oxide phases.[37–42] Growing nanoparticles with well-defined size and structural properties are an essential prerequisite to understand the details of adsorbate-surface interactions and finally the catalytic reaction.

An essential property for technological applications of nanostructures made of magnetic materials such as Fe and Co (e.g., magnetic storage media) is the magnetocrystalline anisotropy energy (MAE), which affects the thermal stability of the collective magnetic moments of nanostructures in the superparamagnetic state.[3–6,11,13–15,17,18] Besides the dependence of the MAE on the material, the size and shape of the clusters are crucial. Many previous investigations show an enhanced MAE and orbital magnetic moment for structures in the subnanometer and nanometer ranges compared to the respective bulk systems due to the lower symmetry of atoms at the surface.[3,4,7,9,10,16] For proper investigations and applications of magnetism at the nanoscale, obtaining clusters with well-aligned easy axes and monodisperse size distribution is a key challenge in order to obtain well-defined magnetic properties.[3–7,13,17] Therefore, a detailed investigation of the morphology and the crystallography is required to understand magnetic and catalytic properties of nanostructures.

In particular, ultrathin alumina on $Ni_3Al(111)$ offers ideal properties for template-mediated growth of self-organized two-dimensional (2D) arrays of clusters. This template is especially useful because it combines large distances between the nucleation sites (4.1 nm) with the possibility to grow three-dimensional clusters, allowing us to tune the cluster size in a range of more than 2 orders of magnitude. The structure of this ≈0.5-nm-thick oxide film, which has been solved recently,[43] exhibits holes reaching down to the metal substrate. These holes, located at the corners of the $(\sqrt{67}\times\sqrt{67})R12.2°$ unit cell, are large enough to trap any kind of metal atoms, but only Pd atoms have been shown to be trapped in these holes so far. The applicability of this alumina film as a template with a 4.1 nm lattice for growing well-ordered metal clusters of Pd and Pd/Au has been noted already before the structure of the oxide was known.[44,45] The unmodified oxide is not a good template for most other metals,[46–48] which was explained by a barrier for other metal atoms preventing them from jumping into these corner holes.[43]

We have shown that the corner holes can be filled with Pd atoms and, hence, a metallic nucleation site can be created where other metal atoms such as Fe and Co can nucleate and form a well-ordered arrangement, too.[43] In the current work, we exploit this method and study the morphology and structure of these clusters in detail.

II. EXPERIMENTAL SETUP

Scanning tunneling microscopy (STM) measurements were carried out in Vienna, in an ultrahigh vacuum (UHV)

system with a base pressure below 10^{-10} mbar. For cleaning the surface of the $Ni_3Al(111)$ crystal, we used 2 keV Ar^+ sputtering and annealing to roughly 1100 K. The cleanliness of the crystal surface was verified by Auger-electron spectroscopy (AES) and STM. As high temperatures would lead to evaporation of Al from the surface, the annealing temperature should not significantly exceed 1100 K. The alumina film was grown at a temperature of 1000 K and an oxygen pressure of $3\times10^{-9}-5\times10^{-9}$ mbar for several hours; this typically corresponds to a dose of ≈40 Langmuir (L; 1 L $=10^{-6}$ torr s). Compared to higher pressures but the same oxygen dose, slower oxidation results in a more homogenous surface, covered with the $(\sqrt{67}\times\sqrt{67})R12.2°$ phase over large areas and fewer domain boundaries. By this preparation procedure, the formation of the other phases, i.e., the "stripe" phase[49] and the hexagonal $(\sqrt{79}\times\sqrt{79})R17°$ oxide phase also observed on this surface,[43] could be avoided. The exact preparation procedure for growth of the desired $(\sqrt{67}\times\sqrt{67})R12.2°$ oxide structure is not exactly the same for all single crystals of nominal composition Ni_3Al; e.g., some crystals may require post annealing at approximately 1150 K after oxidation. As the chemical potential of Al strongly depends on its concentration, we consider it likely that the exact stoichiometry of the crystal plays a role.[43]

Deposition of palladium, cobalt, and iron was done using liquid-nitrogen-cooled electron-beam evaporators (Focus EFM3). High-energy ions have been deflected by a retarding voltage applied at the orifice of the evaporator to avoid creation of defects in the oxide film, which could act as additional nucleation centers for metal atoms.[50] The deposition rate was calibrated by a quartz-crystal microbalance. The coverages stated in this work are readings of the quartz-crystal microbalance, i.e., the film thickness averaged over the sample area, assuming bulk density.

The STM measurements have been obtained at RT in constant current mode using a customized commercial STM (Omicron μ-STM) and an electrochemically etched W tip. In addition to STM, structural properties of Co and Pd clusters were investigated by surface x-ray diffraction (SXRD) in the *surface under ultrahigh vacuum* (SUV) laboratory of the beamline BM32 at the European Synchrotron Radiation Facility (ESRF) in Grenoble. The experimental setup allows us to measure grazing-incidence small-angle x-ray scattering (GISAXS) *in situ* during deposition of the clusters with water-cooled electron-beam evaporators (Focus EFM4) from the onset of cluster formation to coalescence. SXRD and GISAXS measurements were done at a wavelength of $\lambda=62.62$ pm. The incident angle α_i of the x-ray beam for SXRD was 0.5° and for GISXAS measurements 0.2°, very close to the critical angle for total reflection.[51] For these measurements, we have used a crystal well characterized by STM; in addition, prior to the x-ray measurements, the sample preparation was checked with reflection high-energy electron diffraction and AES.

III. OXIDE AND THE ARRANGEMENT OF CLUSTERS ON IT

A. Oxide

The aluminum oxide used in this work as a template for growing well-ordered metal clusters has a $(\sqrt{67}\times\sqrt{67})R12.2°$ unit cell with a $p6$ symmetry [the cell size is given with respect to the 0.5022 nm cell of the ordered $Ni_3Al(111)$ surface].[52] Figure 1 shows two STM images (taken at the same position of the sample) of the alumina film showing (a) the "network" and (b) the "dot" structures, visible at 3.1 and 2.3 V, respectively.[52–54] In both images, two unit cells are drawn. The corners of the unit cells are sixfold symmetry axes of the oxide film and marked by hexagons; the two threefold axes in the cell are marked by triangles in Fig. 1(b). The sixfold sites at the corner of the unit cell are visible as depressions (dark) in the "network structure" or protrusions (bright) in the "dot structure;" these are holes down to the metallic substrate as described above (see Ref. 43 for more details). Also, the threefold sites are defects deviating from the building rules of ultrathin alumina films;[55] there, an Al triangle is found at the metal-oxide interface instead of the usual Al hexagons, with three instead of two interface Al atoms binding to oxygen. Besides the sixfold and threefold sites, the oxide exhibits defects, which are visible in Fig. 1(b) as small bright dots (some marked by circles), less prominent than the corner holes. These extra defects possess no strict long-range order, but they are all close to a threefold axis of the unit cell. While STM images taken at 2.3 V are advantageous to reveal the ordering of the oxide and the extra defects [Fig. 1(b)], we employ STM images taken at 3.1 V to study the geometrical properties of metal clusters grown on top of the oxide (see below).

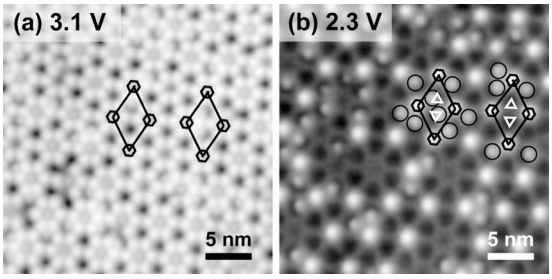

FIG. 1. STM images taken (a) at 3.1 V/0.1 nA where the net structure appears and (b) at 2.3 V/0.1 nA showing the dot structure. The unit cell is drawn in black with the corner holes as hexagons, triangles mark the threefold sites, and circles mark the defects.

B. Fe and Co nucleation on the unmodified oxide

In general, metals on oxide surfaces have a low work of adhesion and clusters growing on oxide films show bad wetting[56] while thin metal films on metal surfaces show good wetting and layer-by-layer growth in many cases.[57] Particularly, it has been shown for the very similar alumina film on NiAl(110) that clusters of many metals exclusively nucleate on defects and at step edges.[27,58–60] Moreover, the high chemical affinity between Al and O atoms should not allow Fe and Co atoms to form a strong bond to any oxygen atom of a defect-free oxygen-terminated alumina surface. Thus, the lowest energy for metal atoms deposited on alumina on $Ni_3Al(111)$ would be in the corner holes, followed by defects.

Figure 2 shows two STM images taken at 3.1 V where (a) 0.1 nm Fe and (d) 0.06 nm Co have been deposited at RT on

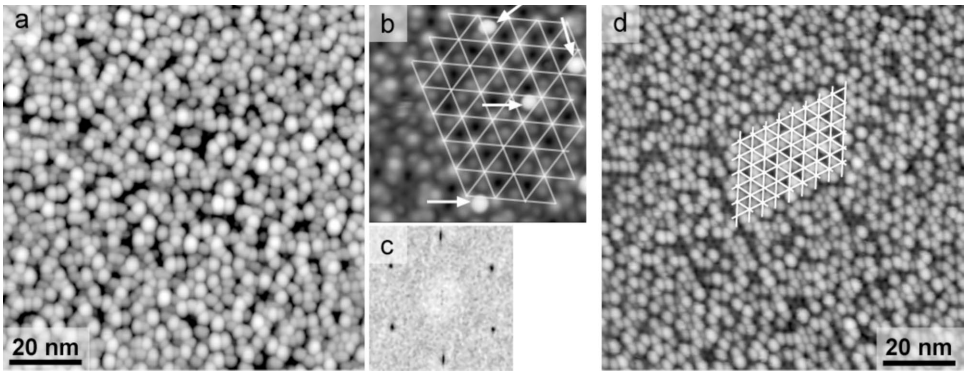

FIG. 2. STM images (3.1 V/0.1 nA) of (a) 0.1 nm Fe and (d) 0.06 nm Co deposited at RT, (b) STM image (2.3 V/0.1 nA) of 0.01 nm Fe where Fe clusters are marked with white arrows, and (c) a Fourier transform of the Fe cluster centers in image (a). The cross points of the white grids in (b) and (d) mark the corner holes.

the clean oxide surface. At first glance, the arrangement of the Fe clusters in Fig. 2(a) seems to be random without any long-range order. Figure 2(b) shows an STM image taken at 2.3 V of 0.01 nm Fe deposited at the same conditions. As mentioned above, at this voltage, the corner holes appear bright and are marked as cross points of the white lattice. The arrows in Fig. 2(b) mark the Fe clusters. It is clearly visible that the nucleation sites of Fe atoms neither match the corner holes nor other high-symmetry positions of the lattice, but their positions are close to the threefold sites. As the position of the clusters and also their number [$\approx 1/2$ of the threefold sites at saturation coverage, Fig. 2(a)] agree with the distribution of the extra defects discussed above, this strongly indicates that the Fe clusters nucleate at these extra defects [circles in Fig. 1(b)].

Figure 2(c) shows a fast Fourier transform (FFT) of a map derived from the STM image shown in Fig. 2(a) where only the cluster centers are marked as points. The sharp spots in the FFT correspond to a distance of $4.1/\sqrt{3}$ nm, i.e., the periodicity of the threefold sites (the "network structure"). This also confirms that the cluster positions are not random. The sharp spots appearing in spite of the poor ordering of the clusters can be explained as follows. Both the partial occupation and random deviations from the threefold site only increase the background, but do not lead to blurring of the spots (this is comparable to the Debye-Waller factor in diffraction).

Figure 2(d) shows Co clusters deposited at RT. Similar to Fe, Co atoms do not nucleate in the corner holes, which are marked as the cross points of the white lattice in Fig. 2(d). Obviously, Co nucleates close to or at almost all the threefold axes of the unit cell, thus it forms a honeycomb lattice, with the corner holes left empty. As Co occupies a larger fraction of the threefold sites, the long-range order of its lattice is more apparent than that of Fe. Thus, Co occupies also regular threefold sites without a nearby defect. As mentioned above, neither Fe nor Co can overcome the barrier to jump into the corner hole at RT.[43]

C. Fe and Co nucleation on the Pd-seeded surface

As mentioned above, in contrast to Fe and Co atoms, Pd atoms are trapped in the corner holes, indicating a small or vanishing barrier for Pd. In Ref. 43, it is demonstrated that the hole is large enough to be filled with three Pd atoms without creating an adatom. These results suggest to create a template with well-ordered metallic dots embedded in the oxide, i.e., the Pd atoms in the corner holes, by predeposition of three Pd atoms per corner hole (three Pd atoms per unit cell; this corresponds to an average coverage of 0.003 nm). If we think of the barrier for Fe or Co atoms as some kind of Ehrlich-Schwoebel barrier at step edges[61,62] [Fig. 3(a)], we can obviously reduce the barrier by filling the holes and thereby allow Fe and Co atoms to nucleate on top of the Pd atoms in the corner holes. From now on, we will refer to the oxide with predeposition of three Pd atoms as Pd seeded. The possibility of seeding the surface with Pd for the growth of ordered nanoparticles has been discovered already before the structure of the oxide was known, but only for Au, a metal that can nucleate at the corner holes without seeding.[45,63]

Our STM experiments have also shown that Pd atoms nucleated in the corner hole become invisible at temperatures above 570 K, which we attribute to diffusion of metal atoms from the bottom of the corner hole into the Ni_3Al bulk or below the aluminum oxide. A similar stability limit is observed for Co clusters grown on the Pd-seeded surface. This observation is in good agreement with Ref. 44, where it was found that deposition at 600 K does not lead to well-ordered Pd clusters at the corner holes. Hence, the deposition temperature is limited to approximately 570 K.

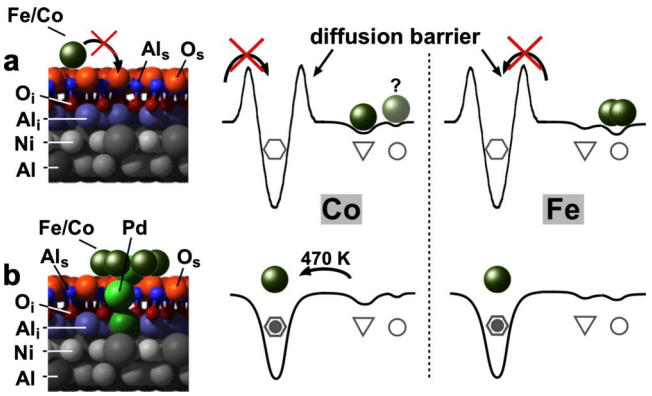

FIG. 3. (Color online) (a) Side view of the corner hole of the oxide with a nearby Fe or Co atom on top. (b) Schematic drawing of the potential-energy surface for Fe as well as Co atoms. Empty hexagons symbolize the corner holes, filled hexagons the corner holes filled by three Pd atoms each, triangles are the threefold sites of the unit cell, and circles are the defects (see also Fig. 1).

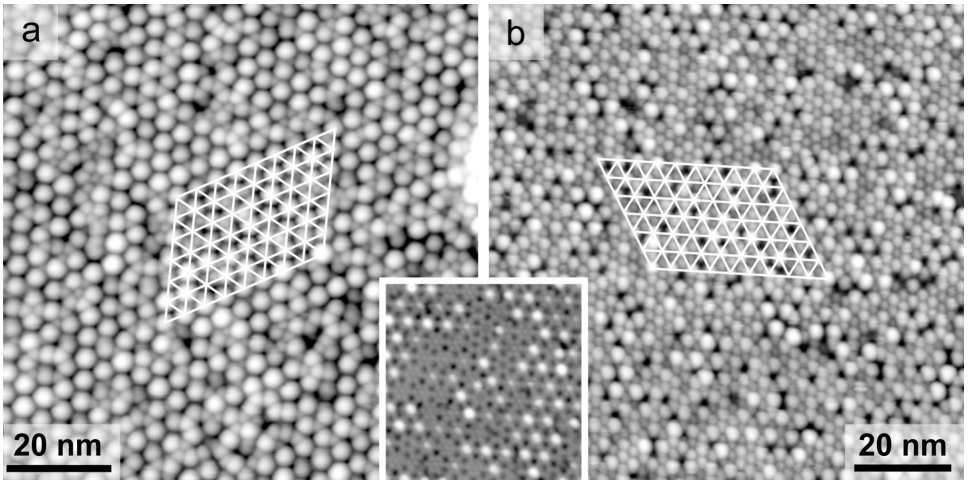

FIG. 4. STM images (3.1 V/0.1 nA) of (a) 0.1 nm Fe and (b) 0.06 nm Co deposited on the Pd-seeded oxide at RT. Cross points of the white grids mark the corner holes. Inset shows an STM image (3.1 V/0.1 nA) of the Pd-seeded oxide. The brightest spots (≈30% of all corner holes) are attributed to holes with at least four Pd atoms; holes filled by two or three Pd atoms appear comparable to or slightly brighter than the surrounding oxide (Ref. 43).

Figure 4 shows two STM images of (a) 0.1 nm Fe clusters and (b) 0.06 nm Co clusters on the Pd-seeded oxide. Pd, Fe, and Co have been deposited at RT. In both cases, Fe as well as Co, a cluster grows on each of the Pd-filled corner holes (cross points of the white lattice). Figure 4(a) shows that Fe clusters now nucleate almost exclusively on top of the corner holes. However, Co clusters now occupy both nucleation sites, the corner holes, and most of the threefold sites of the unit cell [Fig. 4(b)]. Hence, the density of Co clusters is almost 3 times the density of the Fe clusters.

The inset in Fig. 4 shows a STM image of the alumina with holes each filled by three Pd atoms in average and taken at 3.1 V (prior to Fe or Co cluster deposition). In contrast to empty corner holes of the unmodified oxide [dark corner hole, see Fig. 1(a)], filled corner holes appear flat or as protrusions in the STM image (gray or bright). We note that not all corner holes appear equally bright which is easily explicable as the number of Pd atoms will not be exactly 3 in all corner holes. Nevertheless, it seems that the distribution of the number of Pd atoms per corner hole is narrower than a purely statistical (Poisson) distribution. In that case, we would expect 20% of all corner holes to be filled with less than two Pd atoms. Given the atomic diameter of Pd (0.275 nm) and the thickness of the oxide (≈0.5 nm), we consider it very unlikely that a single Pd atom lying deep at the bottom of a corner hole would be sufficient for Co or Fe to overcome the step barrier. After Co or Fe deposition, we find, however, that almost 100% of the corner holes are occupied by clusters (from a statistical distribution of Pd, 80% would be expected). This indicates that the distribution of the number of Pd atoms per corner hole is narrower than a statistical distribution, probably because excess Pd outside the hole (i.e., the fourth Pd atom) is bound more weakly than the Pd in the hole and diffuses to a site with stronger binding. In this scenario, almost all holes are filled with at least two Pd atoms and cluster vacancies (dark spots in the STM images) only appear at defects of the oxide where the corner hole is missing.

We can also use the Pd-seeded oxide as a template at elevated temperatures up to 570 K, where the Pd seeds are still stable (see above). Figure 5 shows 0.1 nm Fe (a) and 0.06 nm Co (b) clusters deposited at 470 K after filling the corner holes with three Pd atoms. Fe clusters deposited at 470 K show good ordering, i.e., they nucleate at the Pd-filled corner holes. This is not very different from the situation found of the RT deposition, apart from fewer clusters nucleated at defects between the corner holes [compare Figs. 4(a) and 5(a)]. Co clusters, nucleating also on top of the threefold sites when deposited at RT, now grow on top of the corner holes only, similar to Fe [Fig. 5(b)]. Hence, the additional kinetic energy of the Co atoms at 470 K is sufficient for

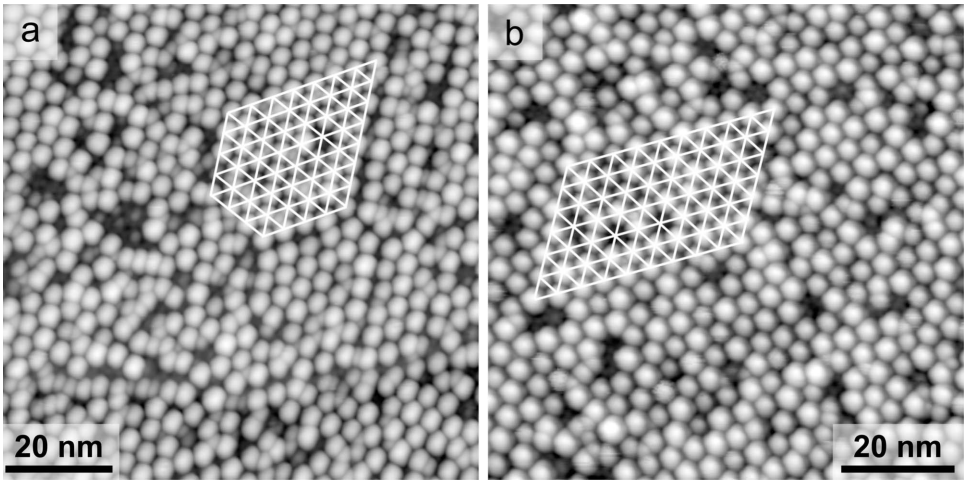

FIG. 5. STM images (3.1 V/0.1 nA) of (a) 0.1 nm Fe and (b) 0.06 nm Co deposited on the Pd-seeded oxide at 470 K. Cross points of the white grids mark the corner holes. In (a), the long-range order is disturbed by domain boundaries of the oxide (e.g., at the right edge of the white grid).

escape from the potential-energy well at the threefold sites and Co nucleation in these sites is suppressed.

By combining the results from above, we can schematically draw the potential-energy surface for Fe and Co adatoms on the clean oxide and the modified oxide with corner holes filled by Pd atoms [Fig. 3(b)]. The corner hole is the deepest well in the potential-energy surface, i.e., the most favorable adsorption site [hexagons in Fig. 3(b)], but only accessible for Fe or Co when filled with Pd atoms (bottom panel; filled hexagons). Without predeposition of Pd, an energy barrier prevents Fe and Co from jumping into the empty corner hole. By filling the corner holes with Pd, the barrier vanishes for Fe and Co. The second best nucleation sites are the defects and the threefold sites [open circles and triangles in Fig. 3(b)]. Nucleation at these sites is different for both metals; obviously the energy minimum at the threefold sites of the ideal oxide structure is too shallow for nucleation of Fe atoms but deep enough to allow Co nucleation at these sites. There are no stable nucleation sites for single Fe atoms on the defect-free unmodified oxide. Also, the defects close to the threefold sites are not very favorable for formation of stable Fe nuclei, i.e., rather shallow minima of the potential energy for Fe adatoms as indicated in Fig. 3(b). As soon as deep sinks for Fe atoms are created by predeposition of Pd, it will be improbable for Fe atoms to meet at the defects on the oxide, which would be required to form a stable nucleus. Therefore, after predeposition of Pd, only few clusters can be found between the corner holes [Fig. 5(a)]. For Co atoms, the threefold sites are stable nucleation sites up to a deposition temperature of about 470 K. We cannot determine the significance of the extra defects for Co. These defects are close to the threefold sites of the unit cell, thus we cannot distinguish between a Co cluster at a threefold site and one at an extra defect. Given the similarity of most properties of Fe and Co, we consider it likely that Co clusters nucleate on these defects instead of the perfect threefold site if a defect is available.

The difference in RT growth between Fe and Co may be related to a deeper potential well for Co at the threefold sites as suggested in Fig. 3(b) and/or it may be the consequence of a different size of the critical nucleus. In the gas phase, bonding in the Co_2 molecule is much stronger (167 kJ/mol) than in Fe_2 (75 kJ/mol); the values on the oxide are probably somewhat lower. This suggests that an Fe_2 dimer on the oxide is not stable at RT while Co_2 should be stable and, hence, creation of a stable nucleus should be easier for Co than for Fe.

D. GISAXS: From well-ordered Co clusters to coalescence

Prior to SXRD (see below), GISAXS measurements were done at the ESRF in Grenoble in order to verify the spatial arrangement of the clusters and, thus, a proper preparation of the aluminum oxide film. The GISAXS data also provide an independent test of the results obtained by STM. Figure 6(a) shows a schematic view of the geometry used for the GISAXS measurements. The GISAXS measurements were done *in situ* during deposition of Co clusters at 470 K on top of the Pd-seeded oxide.

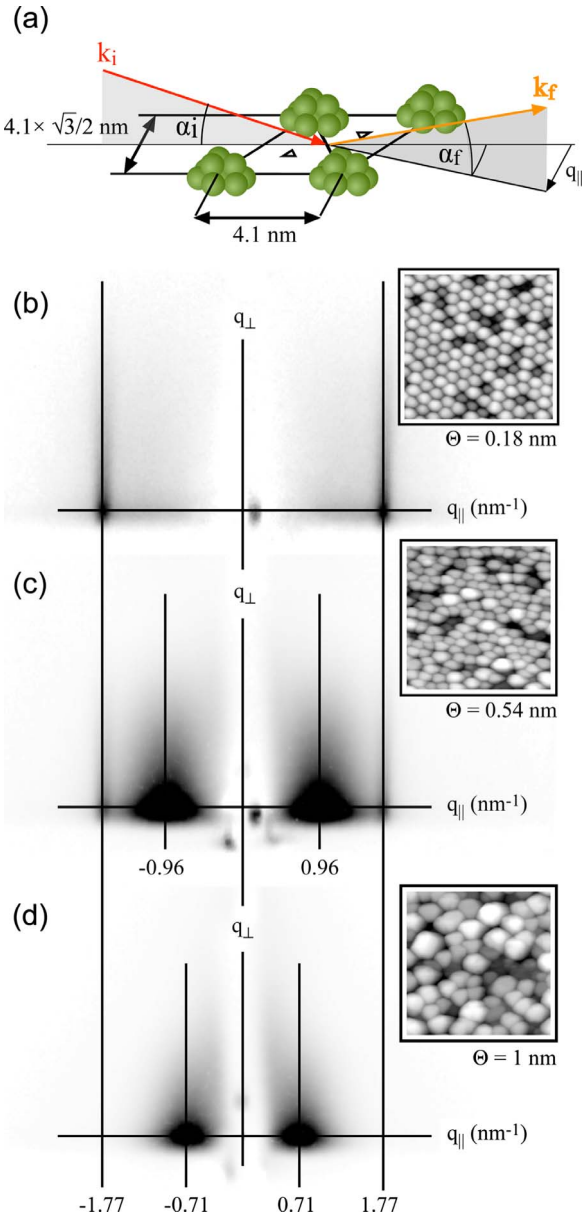

FIG. 6. (Color online) (a) Sketch of the beam alignment with respect to the cluster arrangement in real space. *In situ* GISAXS measurements taken at coverages of (b) Θ=0.18 nm Co, (c) Θ=0.54 nm Co, and (d) Θ=1 nm Co, deposited at 470 K (Pd seeded). The background measured on the Pd-seeded oxide surface prior to deposition has been subtracted leading to some artifacts near the specular beam. Insets are STM images (3.1 V/0.1 nA) taken at equal experimental conditions (50-nm wide each).

Figures 6(b)–6(d) show reciprocal-space images obtained at three different Co coverages; the insets show corresponding STM images acquired in separate experiments with the same growth conditions and the same coverage. Figure 6(b) has been taken at a coverage of 0.18 nm, in the regime of well-ordered cluster growth. The direction of the incident x-ray beam has been aligned in the (11) direction of one superstructure domain, i.e., parallel to a close-packed row of clusters. Therefore, the in-plane coordinate $q_{||}$ of the GISAXS contains the information about the spatial arrange-

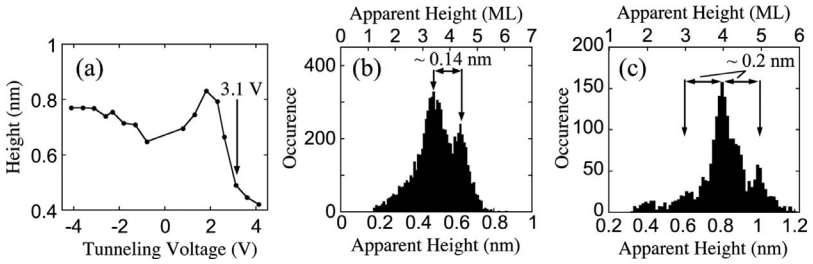

FIG. 7. (a) Apparent average height vs tunneling voltage of 0.06 nm Fe clusters deposited at RT. Height histograms of (b) the same preparation taken at 3.1 V and (c) of 0.1 nm Fe deposited at 570 K. STM images were taken at 0.1 nA; all clusters grown on the Pd-seeded oxide.

ment of the clusters. The two side maxima, found at $q_{\parallel} = \pm 1.77$ nm^{-1} in reciprocal space, correspond to the distance of the rows of clusters, which is $4.1 \times \sqrt{3}/2$ nm in real space [sketch in Fig. 6(a)]. Already at a Co coverage of 0.18 nm, we find a weak background at lower $q_{\parallel}$ [Fig. 6(a)] corresponding to larger distances in real space. This background becomes stronger with increasing coverage. Below coalescence of the well-ordered clusters, this distribution is attributed to areas with badly ordered clusters at domain boundaries or areas with a disordered oxide. The GISXAS measurement shown in Fig. 6(c) was taken at a Co coverage of 0.54 nm, when the correlation peaks of the well-ordered clusters start to diminish. The corresponding STM image shows coalescence of some of the clusters. Due to coarsening, new broad peaks appear at $q_{\parallel} = \pm 0.96$ nm^{-1}. With increasing coverage, these peaks move toward lower $q_{\parallel}$ and broaden due to a loss of correlation. According to STM and GISAXS data, coalescence is completed at a coverage of 1 nm, shown in Fig. 6(d). At this stage, GISAXS as well as Fourier-transformed STM images show a complete loss of the original hexagonal arrangement of the clusters, and the diffraction peak at $q_{\parallel} = \pm 0.71$ nm^{-1} corresponds to a typical distance of clusters in real space of 8.8 nm. This is in good agreement with the result of the STM images taken at the limit of coalescence where the calculated radial autocorrelation function shows a typical distance between the clusters of 9.3 nm.

Line profiles parallel to the $q_{\parallel}$ direction of the correlation peaks in the 2D GISAXS measurements are an indicator of the correlation length and, hence, the domain size. Before coalescence, we find a full width at half maximum (FWHM) of the peaks of roughly 0.1 nm^{-1}. This corresponds to 60 nm in real space, which is in good agreement with the domain size found by STM.

IV. PROPERTIES OF THE CLUSTERS

A. Height distributions of well-ordered Fe and Co clusters

As a first step to determine the morphology of the clusters, we need to measure their height. At low coverages, where the oxide surface between the clusters can be still reached by the STM tip, we can measure the cluster height by STM. Unfortunately, this is not straightforward. If thin layers of insulators are measured by STM, the apparent height of the insulating layer is significantly different from the geometric height[64] and depends on the tunneling voltage.[58,65–67] In particular, for a bias voltage that lies in the band gap of the oxide, the oxide appears thinner than the real thickness, i.e., the tunneling current is low due to a lack of states available for tunneling. We follow the procedure in Ref. 58, where bias-voltage-dependent height measurements have been made in order to determine the geometric heights of the clusters.

Figure 7(a) shows the average height of well-ordered Fe clusters as a function of the tunneling voltage. The clusters were obtained by RT deposition of 0.06 nm Fe, i.e., in average 107 Fe atoms per cluster on the Pd-seeded oxide. The oxide, measured at tunneling voltages in the band gap, will always appear thinner than its geometrical thickness (0.5 nm), therefore the clusters will appear too high in this voltage range. In other words, the maximum apparent height measured for voltages in the band gap is an upper limit of the cluster height. On the other hand, the apparent height of the oxide must be larger than zero and, hence, from Fig. 7(a), we conclude that the real cluster height is in the range of 0.3–0.7 nm. Close to the conduction-band edge, between 2 and 3 V, the apparent height of the oxide increases and thus the apparent height of the clusters decreases. Therefore, we expect an apparent height of the clusters that is close to the real one at voltages near the conduction-band edge. In this work, the STM images were usually acquired at 3.1 V.

Figure 7(b) shows a height histogram of Fe cluster heights measured at 3.1 V [based on the same preparation as Fig. 7(a)]. Two distinct peaks are visible; the peak separation is 0.14 nm, which can be identified as the interlayer distance of Fe bcc (100) planes (0.143 nm). According to the arguments presented above, the apparent height at this voltage must be close to the true cluster height [cf. Fig. 7(a)]. As the peaks must correspond to an integer multiple of the interlayer distance, i.e., 0.14 nm, they could correspond to either 3 and 4 ML or 4 and 5 ML [the top axis of Figs. 7(b) and 7(c) assumes that the apparent height of the oxide at 3.1 V is equal to its true height]. If we assume that the clusters are truncated spheres, for a given height and number of Fe atoms per cluster (107 atoms per cluster), the diameter at the interface of the clusters can be easily calculated.[58] Assuming that the Fe cluster heights of the peaks in Fig. 7(b) correspond to 3 and 4 ML, this calculation would result in an average cluster diameter of 2.6 nm, which is in contradiction to the diameter visible in STM ($<$2.4 nm). For cluster heights of 4 and 5 ML, the calculation results in an average diameter of 2.2 nm, a size that seems to be realistic according to the STM images. Hence, for obtaining the true (geometrical) height of clusters, roughly 0.09 nm has to be added to the apparent height at 3.1 V.

We have also determined the cluster heights of Fe clusters deposited on the Pd-seeded oxide at 570 K [Fig. 7(c)]. In this case, the mean coverage was 0.1 nm, resulting in an average cluster size of 160 Fe atoms per cluster. In contrast to growth

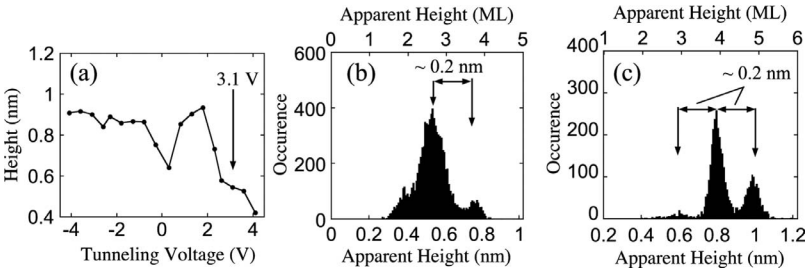

FIG. 8. (a) Apparent average height vs tunneling voltage of 0.06 nm Co clusters deposited at 470 K. Height histograms of (b) the same preparation taken at 3.1 V and (c) of 0.1 nm Co deposited at 570 K. STM images were taken at 0.1 nA; all clusters grown on the Pd-seeded oxide.

at RT, now the distance of the peaks in the clusters height histogram is not 0.14 nm but 0.2 nm, which is close to the interlayer distance of Fe bcc(110) planes (0.202 nm). This means that the crystallographic orientation of the Fe clusters depends on the deposition temperature.

For Co clusters, Fig. 8 shows the voltage dependant height (a) and a height histogram (b) of well-ordered Co clusters obtained by deposition of 0.06 nm at 470 K on the Pd-seeded oxide. This corresponds to an average size of 80 Co atoms per cluster. The average height of the Co clusters measured as a function of the tunneling voltage shows a similar behavior as Fig. 7(a), dominated by the oxide, not the metal. According to Fig. 8(a), the height of the Co clusters is limited to the range of 0.4 up to 0.7 nm. In the height histogram, again measured at 3.1 V tunneling voltage, the peaks are separated by 0.2 nm, which is the interlayer distance of close-packed Co planes, i.e., either fcc(111) or hcp(0001) planes. For well-ordered Co clusters grown on the Pd-seeded oxide with a coverage of 0.1 nm (145 Co atoms per cluster) deposited at 570 K, the same interlayer distance is found [Fig. 8(c)].

In Fig. 8(b), we can assign the main peak to a cluster height either 2 or 3 ML. Repeating the calculation described above, we can exclude 2 ML because the cluster diameter at the interface would be calculated to be 2.6 nm, incompatible with the STM images ($<$2.3 nm). If we assume a thickness of 3 ML for the majority of the clusters [i.e., the main peak in Fig. 8(b)], the result of the calculation is an average cluster diameter of 1.8 nm, so we conclude that this value is the correct one. The difference between the true cluster height and that measured at 3.1 V therefore amounts to 0.07 nm, similar to the one for the Fe clusters shown above.

For metal clusters, we can assume that the difference between true and apparent heights does not strongly depend on the cluster material. Hence, the correction for converting the apparent height measured at 3.1 V bias into a geometric height should be roughly the same for all Fe and Co clusters; the exact value can be determined by the requirement that an integer number of layers should be found. Here, we have neglected a problem caused by the finite resolution of the STM. Small clusters appear lower than the true geometric height because the STM tip follows the local density of states in the vacuum,[68] effectively smearing out the geometrical contours and making small protrusions appear wider, but less high. So we expect that we to have to add a slightly higher correction for small clusters, which have a smaller radius of curvature (smaller top facet), leading to underestimation of the cluster height; conversely, for larger clusters, the correction should be slightly lower. This may explain the fact that the apparent cluster heights of the larger clusters [Figs. 7(c) and 8(c)] are somewhat closer to an integer number of monolayers than those for the smaller ones [Figs. 7(b) and 8(b)].

B. Contact angle of well-ordered Fe and Co clusters

From the known volume of the clusters, i.e., the average number of atoms per cluster, their height, and their density measured by STM, we can calculate the diameters and the contact angles by the equations given in Ref. 58. This calculation assumes that the clusters are truncated spheres, which is a rough approximation for small clusters of a few atomic layers. Nevertheless, the contact angle can be interpreted as a measure of the wetting of the oxide surface by the cluster material. The results for Fe and Co clusters deposited at different coverages and deposition temperatures, all on the Pd-seeded oxide, are given in Table I. We note that the contact angle increases with increasing deposition temperature. This can be easily explained by a higher mobility of Fe and Co atoms at the surface at elevated temperatures, which allows more atoms to jump onto the top terraces of the clusters and thereby the clusters grow higher than at low temperatures. At

TABLE I. Properties of the Fe and Co clusters grown on the Pd-seeded oxide determined from the height distributions. The diameter d is the diameter of the clusters at the oxide-cluster interface.

Cluster material	Fe					Co		
Deposition at T (K)	RT	370	470	470	570	470	470	570
Coverage Θ (nm)	0.06	0.06	0.06	0.1	0.1	0.06	0.1	0.1
Atoms/cluster	107	98	112	161	160	80	145	145
Average height h_{avg} (nm)	0.6	0.7	0.81	0.89	0.84	0.62	0.81	0.85
Contact angle φ	57	73	83	80	79	71	75	82
Diameter d (nm)	2.2	1.84	1.8	2.1	2.2	1.8	1.7	1.8

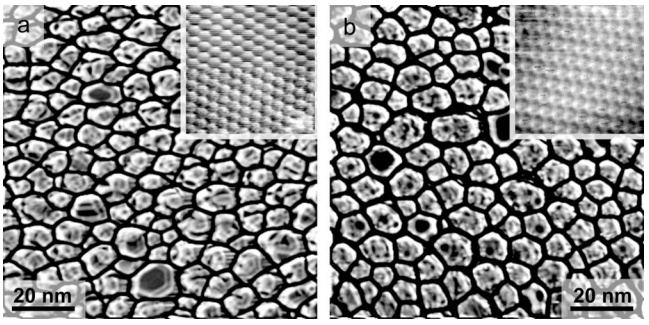

FIG. 9. STM images (3.1 V/0.1 nA) of (a) 2.8 nm Fe and (b) 2.8 nm Co deposited at 470 K (Pd seeded). Images are high-pass filtered to reveal the morphology of the clusters. Insets show STM images (3-nm wide) with atomic resolution from facets on top of flat clusters visible in the large STM images.

constant temperatures, we find that the contact angle does not depend significantly on the cluster size.

We conclude that the contact angle obtained at low temperatures does not correspond to the thermodynamic equilibrium while at higher deposition temperatures, the contact angle approaches the thermodynamic equilibrium; at 570 K, this value is about 80° for both types of clusters, lower than the contact angle of ≈120° found for Co clusters found on NiAl(110).[58] This indicates a higher adhesion energy of the clusters on the oxide on $Ni_3Al(111)$, which might be due to the lower stability (higher surface energy) of this oxide compared to that on NiAl(110).

C. Structure of Fe and Co clusters after coalescence

For small clusters below coalescence, STM with atomic resolution on top of single clusters is not possible due to the high surface curvature. However, for high coverages above coalescence, some of the clusters show flat facets on top where atomic resolution is possible. Figure 9 shows strongly high-pass filtered STM images after deposition of 2.8 nm Fe (a) and Co (b) at 470 K on the Pd-seeded oxide. This coverage is well above the limit of coalescence.

In these STM images, two different cluster species are visible: small distorted clusters with a wrinkled top and a few larger flat clusters. The fraction of flat clusters depends on the temperature of deposition. Below 470 K deposition temperature, small wrinkled Fe or Co clusters are the dominant species while at higher deposition temperatures, larger flat clusters can be seen more frequently. Our explanation for the wrinkled clusters is lattice mismatch of neighboring clusters, e.g., due to different azimuthal orientation of the lattices, leading to polycrystalline clusters upon coalescence. The insets of Fig. 9 are atomically resolved STM images 3-nm wide taken on top of one of the flat clusters visible in the STM images. Both show a surface with roughly sixfold symmetry, i.e., bcc(110) for Fe clusters and a close-packed plane for Co. Hence, the STM images with atomic resolution of clusters above coalescence confirm with the cluster orientation derived from the height histograms of clusters below coalescence.

Unfortunately, STM does not allow us to distinguish between fcc and hcp close-packed Co planes. Hence, SXRD measurements were carried out to clarify this remaining question, which is essential for understanding the magnetic properties.[69–72]

D. Orientation of well-ordered Pd clusters: SXRD and STM

As Pd clusters are easier to prepare and measure by SXRD, due to the higher scattering power of Pd compared to Co, we have started by testing the oxide preparation and the possibility to measure the structural properties of the clusters on well-ordered Pd clusters (confirmed by GISAXS) grown at RT. The Pd coverage was 0.25 nm, below coalescence.

In the following, we label the reflections using the hexagonal cell of $Ni_3Al(111)$ surface as a basis, with the in-plane lattice constant of $a=0.5022$ nm [the $Ni_3Al(111)$ cell being twice as large as its fcc lattice] and $c=0.6151$ in the out-of-plane direction (three layers according to the fcc stacking of Ni_3Al). Figure 10(a) shows an in-plane map of the reciprocal-space, with the reciprocal lattice of the $Ni_3Al(111)$ alloy marked by filled circles. The real-space values corresponding to a given radius in the reciprocal space are indicated at the left.

The Pd clusters grow with an fcc lattice and (111) facets on top; this is confirmed by our XRD data showing a rod at the position marked as "Pd(1,1)," with peaks at $q_\perp=0$ and 27.98 nm^{-1}. A radial scan across this Pd $(1\ 1)_{hex}$ rod at $L=0.06$, i.e., close to the $(-2\ 0\ 2)_{cub}$ Bragg reflection expressed in cubic indices, is shown in Fig. 10(b). From the position of the fitted Gaussian distribution, the in-plane lattice constant can be calculated. We find $d_{Pd\text{-}Pd}=0.273$ nm, which is 0.8% less than the bulk nearest-neighbor distance (0.275 nm). The interlayer spacing derived from our data is 0.2248 nm, the same as in bulk Pd (0.2246) within the error bar. The azimuthal position of the Pd rod is rotated by −24.6° compared to the Ni_3Al $(\bar{1}01)$ direction [i.e., (1 1) in the surface cell reference] and a twin which belongs to the second rotational domain of the oxide can be found rotated by −35.4° (=24.6° −60°) compared to the Ni_3Al $(\bar{1}01)$ direction.

Figure 11 shows a processed STM image of 0.23 nm Pd clusters deposited at RT. The facets on top of the clusters have roughly triangular shape. The Ni_3Al $[\bar{1}01]$ direction is also shown in the figure. The angle between the Ni_3Al $[\bar{1}01]$ direction and the orientation of a typical cluster measured by STM is 25° (the angle has been derived by averaging over facets with similar orientation), a value that agrees with the data obtained from SXRD. We can now identify the angle between the oxide and the Pd clusters to be 12.4°. The orientation of the facets shows some angular spread, however. This is also visible in the SXRD measurements as a broad angular distribution of the Pd $(1\ 1)_{hex}$ Bragg peak.

E. SXRD of Co clusters after coalescence

Assuming that the Co clusters do not change their structural properties upon coalescence, as has been suggested by the STM experiments, SXRD was performed at a Co coverage of 2 nm, above coalescence, to ensure a sufficiently large diffracted intensity and a large number of layers for an unambiguous determination of the rotation of Co clusters

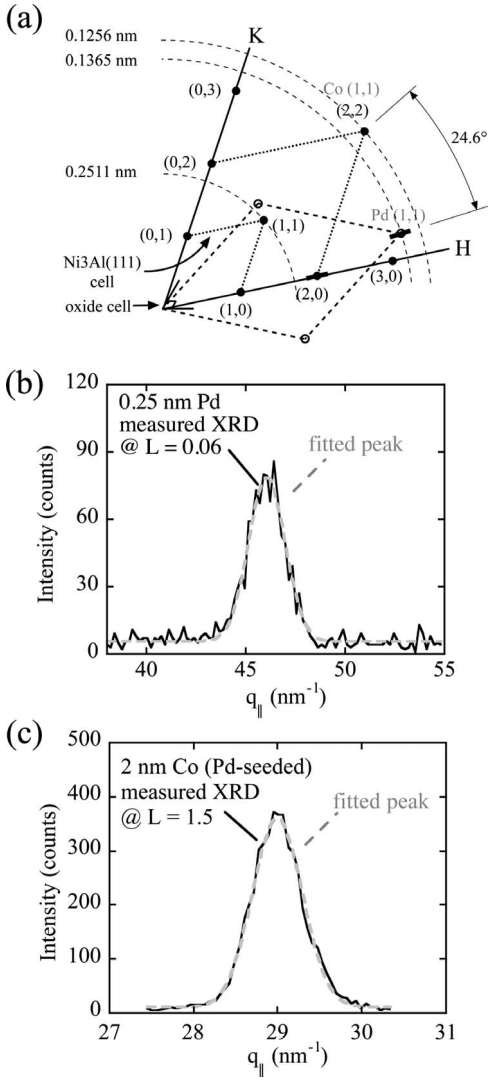

FIG. 10. (a) Map of the reciprocal-space projected onto the surface plane, with Miller indices of the $Ni_3Al(111)$ surface cell. The oxide cell and the Pd as well as the Co hexagonal unit cells are also shown. The radial short thick lines at the Pd $(1\ 1)_{hex}$ and the Co $(1\ 0)_{hex}$ reciprocal-lattice points mark the positions of the scans shown below. (b) Radial XRD scan across the Pd $(1\ 1)_{hex}$ Bragg peak (at $L=0.06$) and (c) radial scan across the Co $(1\ 0)_{hex}$ Bragg peak (at $L=1.5$).

and the type of layer stacking. The clusters were grown at 500 K.

As the nearest-neighbor distance of bulk Co atoms in a close-packed plane ($d_{Co\text{-}Co}=0.2507$ nm) is almost equal to the nearest-neighbor distance of atoms in the $Ni_3Al(111)$ alloy surface (0.2511), the Co $(1\ 0)_{hex}$ rod is located at the same radial distance as the (2 0) rod of the $Ni_3Al(111)$ alloy surface [i.e., the (1 0) rod of the fcc lattice when disregarding the chemical order] [see Fig. 10(a)].

Figure 10(c) shows a radial scan of $q_{\parallel}$, the scattering vector component parallel to the surface, across the (2 0) rod of the substrate at $L=1.5$, where the Co contribution has a maximum (see Sec. IV F). This would correspond to the $(1\ 0)_{hex}$ Bragg peak of hcp Co. An azimuthal scan along the dashed line marked "0.2511 nm" in Fig. 10(a) shows a coincidence of the Co $(1\ 0)_{hex}$ rod with (2 0) rod of the alloy, telling us that the azimuthal orientation of the Co clusters is the same as that of the $Ni_3Al(111)$ surface below the oxide. Due to the finite size of the clusters and to their mosaicity, the angular width of the Co rod is larger than that one of the $Ni_3Al(111)$ crystal truncation rod. Therefore, the radial scan across the Co rod in Fig. 10(c) was actually taken slightly off from the peak maximum [rotated by 0.5° from the (2 0) crystal truncation rod] as shown in Fig. 10(a) (thick short line), minimizing the contribution from the substrate. The in-plane Co lattice constant derived from the fit shown in Fig. 10(c) is 0.2503 nm (0.2% less than in bulk Co).

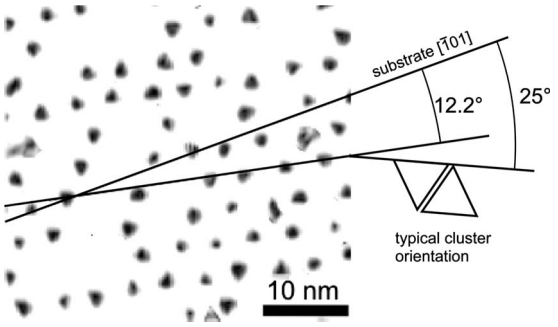

FIG. 11. Processed STM image of Pd clusters deposited at RT ($\Theta=0.23$ nm). A close-packed direction of the substrate has been identified on a large scale STM image from the same experiment where both oxide orientations were present and labeled [$\bar{1}01$]. The typical orientation of the Pd clusters is indicated.

At first glance, an azimuthal orientation of the Co clusters identical to that of the substrate is somewhat unexpected. The corner hole has a diameter of only 0.4 nm, too small for any structure that could transfer the rotational alignment from the substrate to the cluster, and also the ring of Al and O atoms directly surrounding the corner hole is not rotationally aligned with a low-index direction of the substrate. We note, however, that the oxide around the corner holes has rows of O and Al atoms deviating by about 2° or less from the $\langle 1\ 1\ \bar{2}\rangle$ directions of the substrate. The distance between these rows is typically around 0.25 nm, thus it fits the Co-Co interatomic spacing, but not the distance between Co rows in a close-packed Co layer (0.217 nm). An overlayer with Co-Co neighbors aligned in the direction of the 0.25 nm vectors in the oxide will have an azimuthal orientation roughly parallel to the Ni_3Al substrate. Of course, this is not a coincidence. The orientation and distance of the O and Al rows in the oxide surface are due to the registry of the lower layers in the oxide on the Ni_3Al substrate.

F. Layer stacking of Co clusters after coalescence

Knowing the azimuthal orientation of the Co clusters, we can now proceed to study the layer stacking of the Co clusters. Figure 12(a) shows a scan along the $(1\ 0)_{hex}$ Co rod. Again the scan was performed at an azimuth 0.5° off the crystal truncation rod to increase the ratio of the desired Co signal to the (in this measurement) interfering substrate rod. The large peak at $q_{\perp}=10.2\ nm^{-1}$ can be identified as the (2 0 1) Bragg peak of the $Ni_3Al(111)$ alloy (using the hexago-

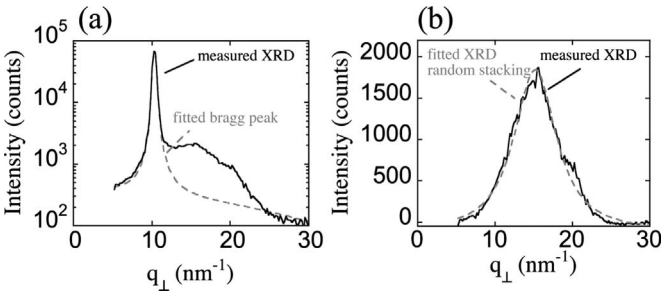

FIG. 12. (2 0) rod of the surface after deposition of 2 nm Co clusters deposited at 470 K (Pd seeded). (a) With the Bragg peak of $Ni_3Al(111)$ at $q_\perp = 10.2$ nm^{-1} ($L=1$) fitted by a pseudo-Voigt function (dashed) and (b) after Bragg peak subtraction. This corresponds to the $(1\ 0)_{hex}$ rod of a Co hcp (0001) or fcc(111) surface. The peak is fit for random stacking of close-packed planes.

nal basis). The dashed gray line shows a pseudo-Voigt fit of the Bragg peak. After subtracting this fitted bulk peak, a peak at $q_\perp = 15.1$ nm^{-1} remains [Fig. 12(b)]. This peak can be fitted by

$$I(q) = \frac{C}{5/4 + \cos(qd)},$$

a function that describes the scattering power of close-packed planes with random stacking and an interlayer distance d (Ref. 73) [dashed in Fig. 10(b)]. The peak in Fig. 12(b) results in $d=0.206$ nm, the interlayer distance of close-packed Co planes (0.2035 nm for Co hcp). This confirms the interlayer distance observed in the STM height histograms. Hence, we conclude that Co clusters on top of the corner holes grow with roughly the same azimuthal orientation as the $Ni_3Al(111)$ surface below the oxide and with random stacking of close-packed planes.

V. SUMMARY

We have demonstrated the applicability of alumina on $Ni_3Al(111)$ as a template with a 4.1 nm lattice for growing highly ordered clusters of Co as well as Fe. Pd atoms trapped in the corner holes of the oxide create metallic nucleation sites where Fe or Co can nucleate and form a well-ordered hexagonal arrangement on the oxide nanomesh. We have studied the morphology of these Fe and Co clusters and applied different methods such as STM, XRD, and GISAXS to determine the morphology and crystallographic properties of the clusters.

Fe clusters grow exclusively on top of the Pd atoms in the corner holes at temperatures ranging from RT up to 570 K. Co clusters deposited at RT nucleate at the Pd-filled corner holes, but also on a second site with threefold symmetry. Nucleation on these threefold sites can be avoided by deposition at or above 470 K, where also Co nucleates exclusively on top of the Pd atoms in the corner holes. As shown for Fe clusters without predeposition of Pd, our study also demonstrates that sharp spots in the Fourier transform of the cluster positions do not imply good ordering of the clusters. We explain the differences of cluster growth with and without Pd seeds in the corner holes by an energy barrier for diffusion of Fe and Co atoms into the corner holes. This energy barrier is small or vanishes for Pd atoms, allowing them to jump into the corner hole, which is the energetically most favorable nucleation site. The distance between the clusters of 4.1 nm, rather large for self-organized templates, and the high contact angles makes it possible to grow fairly large clusters ($\approx$1000 atoms) before coalescence occurs and the high degree of ordering disappears.

Fe clusters deposited at RT grow with bcc (100) planes parallel to the substrate surface; clusters grown at elevated temperatures (above 470 K) have bcc (110) orientation. Co clusters exhibit close-packed planes on top in the temperature range for growing well-ordered clusters (470–570 K). XRD measurements have shown that these Co clusters are neither fcc nor hcp but possess random stacking of close-packed planes; the azimuthal orientation is close to that of the substrate. Finally, Pd clusters grow with their fcc(111) planes on top; their azimuthal orientation is rotated 24.6° with respect to the substrate (12.4° with respect to the oxide unit cell).

ACKNOWLEDGMENTS

This work was financially supported by the Austrian Fonds zur Förderung der wissenschaftlichen Forschung. Beam time at ESRF is acknowledged.

[1] P. Ohresser, N. B. Brookes, S. Padovani, F. Scheurer, and H. Bulou, Phys. Rev. B **64**, 104429 (2001).
[2] B. D. Terris and T. Thomson, J. Phys. D **38**, R199 (2005).
[3] N. Weiss, T. Cren, M. Epple, S. Rusponi, G. Baudot, S. Rohart, A. Tejeda, V. Repain, S. Rousset, P. Ohresser, F. Scheurer, P. Bencok, and H. Brune, Phys. Rev. Lett. **95**, 157204 (2005).
[4] S. Rohart, V. Repain, A. Tejeda, P. Ohresser, F. Scheurer, P. Bencok, J. Ferre, and S. Rousset, Phys. Rev. B **73**, 165412 (2006).
[5] J. Y. Yang, K. S. Yoon, Y. H. Do, J. H. Kim, J. H. Lee, C. O. Kim, J. P. Hong, and E. K. Kim, IEEE Trans. Magn. **41**, 3313 (2005).
[6] C. Petit, S. Rusponi, and H. Brune, J. Appl. Phys. **95**, 4251 (2004).
[7] H. Brune, *Physics and Engineering of New Materials* (Springer, Berlin, 2009), Vol. 127, p. 123.
[8] H. Brune and P. Gambardella, Surf. Sci. **603**, 1812 (2009).
[9] G. Moulas, A. Lehnert, S. Rusponi, J. Zabloudil, C. Etz, S. Ouazi, M. Etzkorn, P. Bencok, P. Gambardella, P. Weinberger, and H. Brune, Phys. Rev. B **78**, 214424 (2008).
[10] P. Gambardella, S. Rusponi, M. Veronese, S. S. Dhesi, C. Grazioli, A. Dallmeyer, I. Cabria, R. Zeller, P. H. Dederichs, K. Kern, C. Carbone, and H. Brune, Science **300**, 1130 (2003).
[11] T. Cren, S. Rusponi, N. Weiss, M. Epple, and H. Brune, J. Phys.

Chem. B **108**, 14685 (2004).
[12] H. Brune and S. Rusponi, Chem. Phys. Solid Surf. **12**, 427 (2007).
[13] S. I. Woods, J. R. Kirtley, S. Sun, and R. H. Koch, Phys. Rev. Lett. **87**, 137205 (2001).
[14] C. Petit, A. Taleb, and M. P. Pileni, Adv. Mater. **10**, 259 (1998).
[15] V. F. Puntes, K. M. Krishnan, and P. Alivisatos, Appl. Phys. Lett. **78**, 2187 (2001).
[16] C. Antoniak, J. Lindner, M. Spasova, D. Sudfeld, M. Acet, M. Farle, K. Fauth, U. Wiedwald, H. G. Boyen, P. Ziemann, F. Wilhelm, A. Rogalev, and S. Sun, Phys. Rev. Lett. **97**, 117201 (2006).
[17] S. Sun, C. B. Murray, D. Weller, L. Folks, and A. Moser, Science **287**, 1989 (2000).
[18] W. Wernsdorfer, E. B. Orozco, K. Hasselbach, A. Benoit, B. Barbara, N. Demoncy, A. Loiseau, H. Pascard, and D. Mailly, Phys. Rev. Lett. **78**, 1791 (1997).
[19] A. T. Bell, Science **299**, 1688 (2003).
[20] C. R. Henry, Surf. Sci. Rep. **31**, 231 (1998).
[21] C. T. Campbell, Surf. Sci. Rep. **27**, 1 (1997).
[22] M. Haruta, N. Yamada, T. Kobayashi, and S. Iijima, J. Catal. **115**, 301 (1989).
[23] M. Haruta, T. Kobayashi, H. Sano, and N. Yamada, Chem. Lett. **16**, 405 (1987).
[24] M. Moreno-Manas and R. Pleixats, Acc. Chem. Res. **36**, 638 (2003).
[25] H. P. Kormann, G. Schmid, K. Pelzer, K. Philippot, and B. Chaudret, Z. Anorg. Allg. Chem. **630**, 1913 (2004).
[26] M. Yashima, L. K. L. Falk, A. E. C. Palmqvist, and K. Holmberg, J. Colloid Interface Sci. **268**, 348 (2003).
[27] M. Heemeier, A. F. Carlsson, M. Naschitzki, M. Schmal, M. Baumer, and H.-J. Freund, Angew. Chem., Int. Ed. **41**, 4073 (2002).
[28] S. Schauermann, J. Hoffmann, V. Johánek, J. Hartmann, J. Libuda, and H.-J. Freund, Angew. Chem., Int. Ed. **41**, 2532 (2002).
[29] S. Sun and C. B. Murray, J. Appl. Phys. **85**, 4325 (1999).
[30] K. Aït-Mansour, A. Buchsbaum, P. Ruffieux, M. Schmid, P. Grning, P. Varga, R. Fasel, and O. Gröning, Nano Lett. **8**, 2035 (2008).
[31] S. Berner, M. Corso, R. Widmer, O. Groening, R. Laskowski, P. Blaha, K. Schwarz, A. Goriachko, H. Over, S. Gsell, M. Schreck, H. Sachdev, T. Greber, and J. Osterwalder, Angew. Chem., Int. Ed. **46**, 5115 (2007).
[32] M. Corso, W. Auwärter, M. Muntwiler, A. Tamai, T. Greber, and J. Osterwalder, Science **303**, 217 (2004).
[33] H. Brune, M. Giovannini, K. Bromann, and K. Kern, Nature (London) **394**, 451 (1998).
[34] T. Classen, G. Fratesi, G. Costantini, S. Fabris, F. L. Stadler, C. Kim, S. de Gironcoli, S. Baroni, and K. Kern, Angew. Chem., Int. Ed. **44**, 6142 (2005).
[35] S. W. Kim, S. U. Son, S. S. Lee, T. Hyeon, and Y. K. Chung, Chem. Commun. (Cambridge) **2001**, 2212.
[36] K. H. Park, S. U. Son, and Y. K. Chung, Org. Lett. **4**, 4361 (2002).
[37] R. Burch, Catal. Rev. **46**, 271 (2004).
[38] K. Shimizu and A. Satsuma, Phys. Chem. Chem. Phys. **8**, 2677 (2006).
[39] H. Over, O. Balmes, and E. Lundgren, Surf. Sci. **603**, 298 (2009).
[40] B. L. M. Hendriksen and J. W. M. Frenken, Phys. Rev. Lett. **89**, 046101 (2002).
[41] R. Westerström, J. G. Wang, M. Ackermann, J. Gustafson, A. Resta, A. Mikkelsen, J. N. Andersen, E. Lundgren, O. Balmes, X. Torrelles, J. W. M. Frenken, and B. Hammer, J. Phys.: Condens. Matter **20**, 184018 (2008).
[42] G. Rupprechter and C. Weilach, J. Phys.: Condens. Matter **20**, 184019 (2008).
[43] M. Schmid, G. Kresse, A. Buchsbaum, E. Napetschnig, S. Gritschneder, M. Reichling, and P. Varga, Phys. Rev. Lett. **99**, 196104 (2007).
[44] S. Degen, C. Becker, and K. Wandelt, Faraday Discuss. **125**, 343 (2004).
[45] G. Hamm, C. Becker, and C. R. Henry, Nanotechnology **17**, 1943 (2006).
[46] C. Becker, A. Rosenhahn, A. Wiltner, K. von Bergmann, J. Schneider, P. Pervan, M. Milun, M. Kralj, and K. Wandelt, New J. Phys. **4**, 75 (2002).
[47] C. Becker, K. von Bergmann, A. Rosenhahn, J. Schneider, and K. Wandelt, Surf. Sci. **486**, L443 (2001).
[48] A. Lehnert, A. Krupski, S. Degen, K. Franke, R. Decker, S. Rusponi, M. Kralj, C. Becker, H. Brune, and K. Wandelt, Surf. Sci. **600**, 1804 (2006).
[49] S. Gritschneder, S. Degen, C. Becker, K. Wandelt, and M. Reichling, Phys. Rev. B **76**, 014123 (2007).
[50] C. Nagl, O. Haller, E. Platzgummer, M. Schmid, and P. Varga, Surf. Sci. **321**, 237 (1994).
[51] B. L. Henke, E. M. Gullikson, and J. C. Davis, At. Data Nucl. Data Tables **54**, 181 (1993).
[52] S. Degen, A. Krupski, M. Kralj, A. Langner, C. Becker, M. Sokolowski, and K. Wandelt, Surf. Sci. **576**, L57 (2005).
[53] A. Rosenhahn, J. Schneider, C. Becker, and K. Wandelt, J. Vac. Sci. Technol. A **18**, 1923 (2000).
[54] T. Maroutian, S. Degen, C. Becker, K. Wandelt, and R. Berndt, Phys. Rev. B **68**, 155414 (2003).
[55] M. Schmid, M. Shishkin, G. Kresse, E. Napetschnig, P. Varga, M. Kulawik, N. Nilius, H.-P. Rust, and H.-J. Freund, Phys. Rev. Lett. **97**, 046101 (2006).
[56] N. Eustathopoulos and B. Drevet, J. Phys. III **4**, 1865 (1994).
[57] H. Brune, *Landolt Börnstein Series: Physics of Covered Solid Surfaces* (Springer, Berlin, 2001), Vol. 42A, p. 217.
[58] E. Napetschnig, M. Schmid, and P. Varga, Surf. Sci. **601**, 3233 (2007).
[59] T. Worren, K. Højrup Hansen, E. Lægsgaard, F. Besenbacher, and I. Stensgaard, Surf. Sci. **477**, 8 (2001).
[60] M. Bäumer, M. Frank, M. Heemeier, R. Kühnemuth, S. Stempel, and H.-J. Freund, Surf. Sci. **454-456**, 957 (2000).
[61] G. Ehrlich and F. G. Hudda, J. Chem. Phys. **44**, 1039 (1966).
[62] R. L. Schwoebel and E. J. Shipsey, J. Appl. Phys. **37**, 3682 (1966).
[63] M. Marsault, G. Hamm, A. Wörz, G. Sitja, C. Barth, and C. R. Henry, Faraday Discuss. **138**, 407 (2008).
[64] W. Hebenstreit, J. Redinger, Z. Horozova, M. Schmid, R. Podloucky, and P. Varga, Surf. Sci. **424**, L321 (1999).
[65] K. Højrup Hansen, T. Worren, E. Lægsgaard, F. Besenbacher, and I. Stensgaard, Surf. Sci. **475**, 96 (2001).
[66] D. C. Lim, I. Lopez-Salido, R. Dietsche, M. Bubek, and Y. D. Kim, Chem. Phys. **330**, 441 (2006).
[67] Th. Bertrams, A. Brodde, and H. Neddermayer, J. Vac. Sci. Technol. B **12**, 2122 (1994).

[68] J. Tersoff and D. R. Hamann, Phys. Rev. B **31**, 805 (1985).
[69] D. Weller, G. R. Harp, R. F. C. Farrow, A. Cebollada, and J. Sticht, Phys. Rev. Lett. **72**, 2097 (1994).
[70] D. Weller, A. Carl, R. Savoy, T. C. Huang, M. F. Toney, and C. Chappert, J. Phys. Chem. Solids **56**, 1563 (1995).
[71] G. R. Harp, R. F. C. Farrow, D. Weller, T. A. Rabedeau, and R. F. Marks, Phys. Rev. B **48**, 17538 (1993).
[72] S. Park, X. Zhang, A. Misra, J. D. Thompson, M. R. Fitzsimmons, S. Lee, and C. M. Falco, Appl. Phys. Lett. **86**, 042504 (2005).
[73] A. Guinier, *X-Ray Diffraction in Crystals, Imperfect Crystals, and Amorphous Bodies* (Dover, New York, 1994), p. 230.